Supplementary materials

Section 1: Bell-CHSH Inequality Test

The Bell–CHSH inequality provides a powerful means of distinguishing quantum entanglement from classical correlations. In our experiment, we conducted a full Bell test based on the Clauser–Horne–Shimony–Holt (CHSH) formulation[1], employing polarization-entangled photon pairs. The experimental configuration and measurement procedure were inspired by the seminal work of Weihs *et al*[2].

The experiment involved two spatially separated observers, Alice and Bob, each independently selecting one of two measurement settings corresponding to distinct polarization analyzer orientations. For polarization-entangled states, quantum mechanics predicts correlations between their measurement outcomes that can violate the CHSH inequality.

For any pair of analyzer settings $(\alpha,\ \beta)$, the normalized correlation function $E(\alpha,\beta)$ is defined as:

$$E(\alpha,\beta)=\frac{N_{++}(\alpha,\beta)+N_{--}(\alpha,\beta)-N_{\pm}(\alpha,\beta)-N_{\mp}(\alpha,\beta)}{N_{++}(\alpha,\beta)+N_{--}(\alpha,\beta)+N_{\pm}(\alpha,\beta)+N_{\mp}(\alpha,\beta)} \tag{1}$$

where N_{ij} represents the coincidence counts for Alice's outcome i and Bob's outcome j, with $+$ and $-$ representing projections parallel and orthogonal to the selected analyzer angle, respectively.

The Bell-CHSH parameter S is then calculated from four correlation measurements at specific angle configurations:

$$S = |E(\alpha,\ \beta) - E(\alpha',\ \beta)| + |E(\alpha,\ \beta') + E(\alpha',\ \beta')| \quad (2)$$

Quantum mechanics predicts violations of Bell's inequality for certain combinations of analyzer orientations. In particular, maximal violation is achieved using the angle settings 0°, 45°, 22.5°, and 67.5°. By inputting the coincidence count data from Table 1 into Eq. (1), we obtained the correlation values presented in Table 2. Subsequent substitution of these values into Eq. (2) yielded a Bell parameter of $S = 2.662 \pm 0.006$, demonstrating clear violation of the classical bound.

Section 2: Target Object Details

This section presents the phase-only object pattern (the "flower" pattern) demonstrated in the main text. The phase of the "flower" structure increases incrementally from 0 (core) to π (background), with a gradient of $\frac{\pi}{6}$, resulting in six discrete phase levels. Using a commercial finite-difference time-domain (FDTD) solver, we numerically simulated the phase sample. The dimensions of the cylindrical α-Si nanopillars were designed to meet the phase requirements of each "flower" region, followed by etching into a silica SiO_2 substrate. A monitor was placed above the pillar array, while the light source was positioned below the substrate. This configuration ensured that incident light accumulated spatially varying phase shifts through the nanopillars. The region above the substrate (unmodulated by the metasurface) is air under identical conditions. The monitor and light source were positioned at distances L_m and L_s from the metasurface, respectively. The phase detected by the monitor is denoted as φ_m, with the substrate refractive index set to 1.5. The phase difference ($\Delta\varphi$) between modulated and unmodulated fields induced by the nanostructure is expressed as:

$$\Delta\varphi = \varphi_m - \frac{2\pi}{\lambda}(L_m + 1.5L_s)$$

Using the above equation, we calculate the phase difference ($\Delta\varphi$) for six dielectric pillars with radii of 181 nm, 200 nm, 228 nm, 242nm, 264 nm, and 153 nm (comma added for list clarity). The height of each pillar is fixed at 500 nm, and the lattice periodicity of the nanostructures is 400 nm. All six pillars exhibit high transparency, ensuring no intensity modulation of the optical field.

The fabricated phase pattern is shown in Fig. S1, where yellow, light pink, dark pink, light green, dark green, and blue regions correspond to nanopillars with phase differences ($\Delta\varphi$) of 0, $\frac{\pi}{5}$, $\frac{2\pi}{5}$, $\frac{3\pi}{5}$, $\frac{4\pi}{5}$, $\frac{5\pi}{5}$ and π respectively. The nanopillars are arranged in a 320 × 320 array. Owing to the rotational symmetry of the nanopillars, the phase distribution is polarization-independent.

We emphasize that this phase object (the "flower" pattern) serves exclusively as a proof-of-concept demonstration. Crucially, our proposed reconstruction method requires no prior knowledge of the sample's phase distribution.

Section 3: Simulation of Imaging Performance under Different Illumination Conditions

To further validate the applicability and robustness of the proposed imaging scheme in practical scenarios, we performed systematic numerical simulations under various illumination conditions. Specifically, we compared the system's performance using both plane wave and Gaussian beam illumination (beam waist $w_0 = 0.5$ mm) , with a fixed wavelength of 780 nm. The test sample was a representative “flower” phase structure.

As shown in Fig. S2, the imaging results under both bright-field and dark-field configurations exhibit high contrast and image quality, regardless of whether the illumination is a Gaussian beam or a plane wave. This confirms that the proposed method is highly robust with respect to the spatial profile of the input beam and is well-suited for diverse experimental conditions.

In addition, we evaluated the sensitivity of the system to variations in the incident angle. Simulations were conducted by introducing small angular deviations to the incident plane wave. As illustrated in Fig. S3, the imaging performance remains stable when the incident angle deviates by less than $\pm 0.05°$, with negligible degradation in image quality. However, larger angular deviations lead to a noticeable decrease in contrast and resolution. These results indicate that while the system is tolerant to different types of illumination beams, it is relatively sensitive to the incident angle and requires precise angular alignment in practical implementations.

In summary, the proposed imaging scheme demonstrates strong versatility with respect to beam type, and emphasizes the importance of angular precision to ensure optimal performance.

Section 4: Robustness Evaluation of Bright-Dark Phase Contrast Imaging Method for Arbitrary Phase Distributions

To evaluate the robustness and general applicability of our phase imaging method, we conducted numerical simulations using Gaussian beam illumination (λ = 780 nm, beam waist = 0.5 mm). Two types of phase samples were tested: (1) uniform phase-gradient objects (Fig. S4) as idealized models, and (2) complex samples with randomized phase profiles (Fig. S5), mimicking biological tissue structures.

The results show that our method ensures high-contrast imaging in at least one mode, enabling observation of biological cells with complex phase structures regardless of their phase complexity. This demonstrates strong adaptability and broad potential for biomedical applications such as cell morphology analysis, tissue diagnostic, laying a solid foundation for future advances in phase imaging of complex biological specimens.

Table 1 Coincidence Measurements for Evaluation of Bell Inequality

Polarizer Angle	**N**			
Bob **Alice**	**22.5°** （+）	**112.5°** （-）	**-22.5°** （+）	**67.5°** （-）
0° （+）	2438	13148	3165	13578
90° （-）	16452	4113	17420	2607
45° （+）	17435	1888	4135	14901
-45° （-）	5014	13782	18584	1772

Table 2 Correlation Measurements for Calculation of the Bell-CHSH Parameter

Polarizer Angle/(°)	**E**	**ΔE**
0, 22.5	-0.638	0.002
0, 67.5	0.638	0.004
45, 22.5	-0.686	0.002
45, 67.5	-0.700	0.003

Fig. S1 Phase object

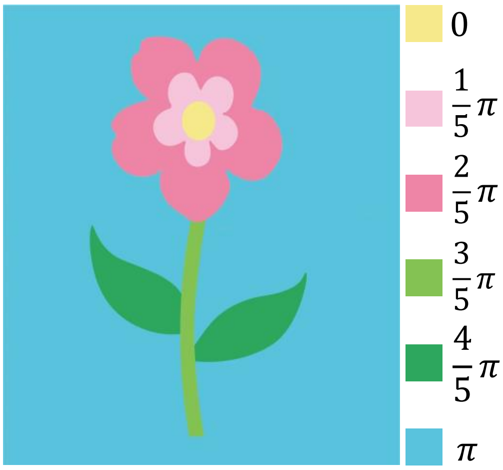

Fig. S1 Phase distribution of the "flower" pattern. The pattern consists of multiple spatial regions with distinct phase shifts, represented using color coding. Specifically, the yellow core corresponds to a phase shift of 0, followed by the light pink first petal layer with a phase of $\pi/5$, and the darker pink second petal layer with $2\pi/5$. The light green stems carry a phase of $3\pi/5$, while the dark green leaves represent $4\pi/5$. The surrounding blue background completes the structure with a phase shift of π. This well-defined, layered phase distribution serves as a structured and interpretable test sample for evaluating the system's phase sensitivity and spatial resolution.

Fig. S2 Bright-dark phase contrast imaging effects under different types of incident illumination.

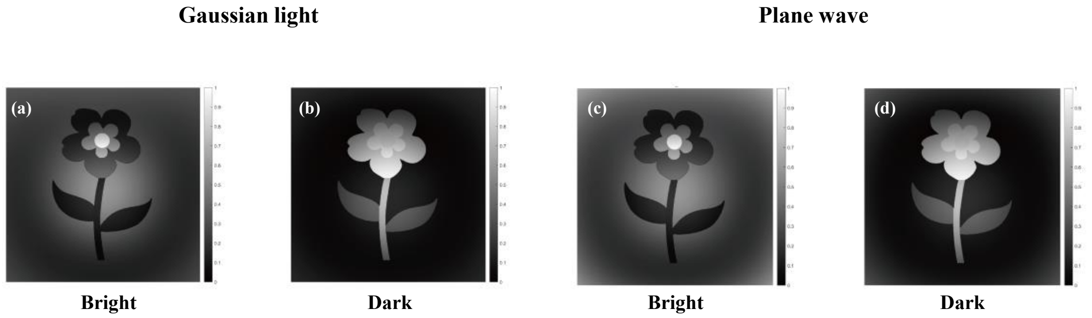

Fig.S2 Phase contrast imaging results of the "flower" sample under different types of illumination conditions: (a) bright-field and (b) dark-field images under Gaussian beam illumination (beam waist w_0 = 0.5 mm); (c) bright-field and (d) dark-field images under plane-wave illumination (λ = 780 nm).

Fig. S3 Sensitivity of imaging performance to incident angle deviations in Gaussian beam illumination.

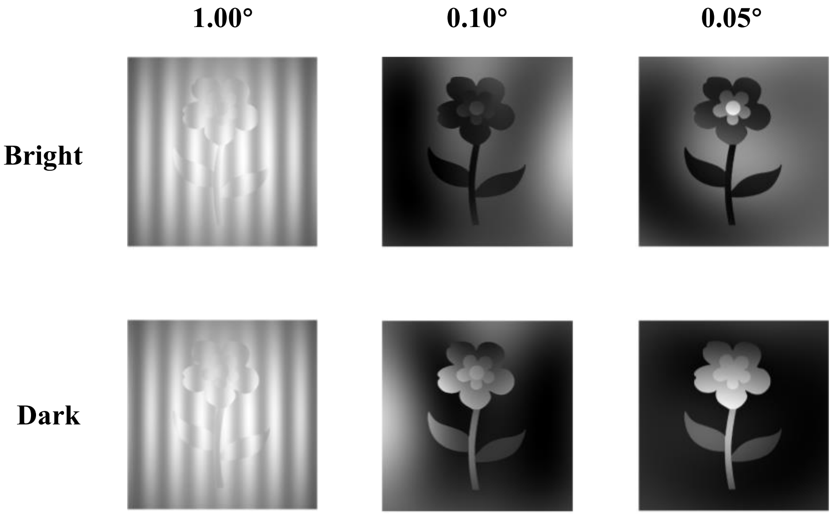

Fig.S3 Phase contrast images were simulated with Gaussian beam illumination. From left to right, the incident angles are 1.00°, 0.10°, and 0.05°. Imaging quality decreases noticeably at larger angles but remains stable within ±0.05°. This demonstrates the system’s sensitivity to incident angle alignment.

Fig. S4 Imaging simulation with varying constant phase gradients

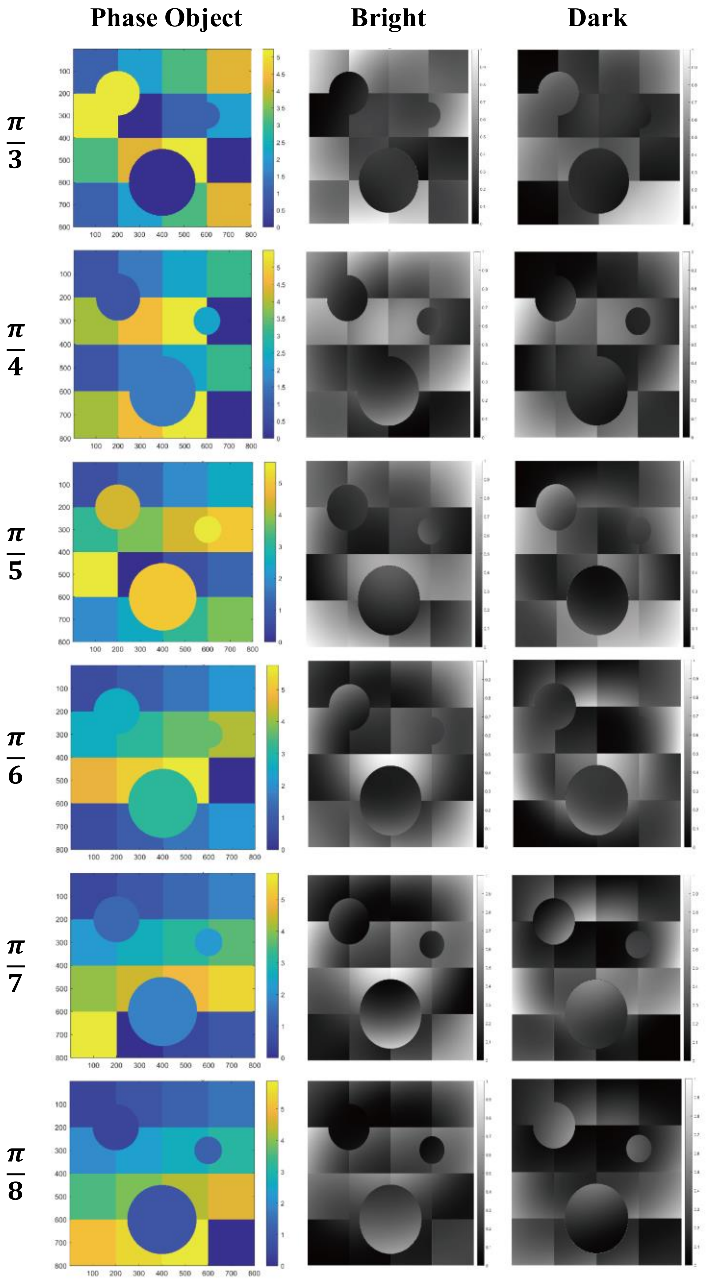

Fig. S4 Simulated bright-field and dark-field phase-contrast imaging of pure-phase objects with uniform phase gradients ($\frac{\pi}{3}$, $\frac{\pi}{4}$, $\frac{\pi}{5}$, $\frac{\pi}{6}$, $\frac{\pi}{7}$, and $\frac{\pi}{8}$). The simulation results demonstrate that our method achieves consistent contrast performance across all tested phase gradients.

Fig. S5 Imaging simulation with arbitrary phase distributions

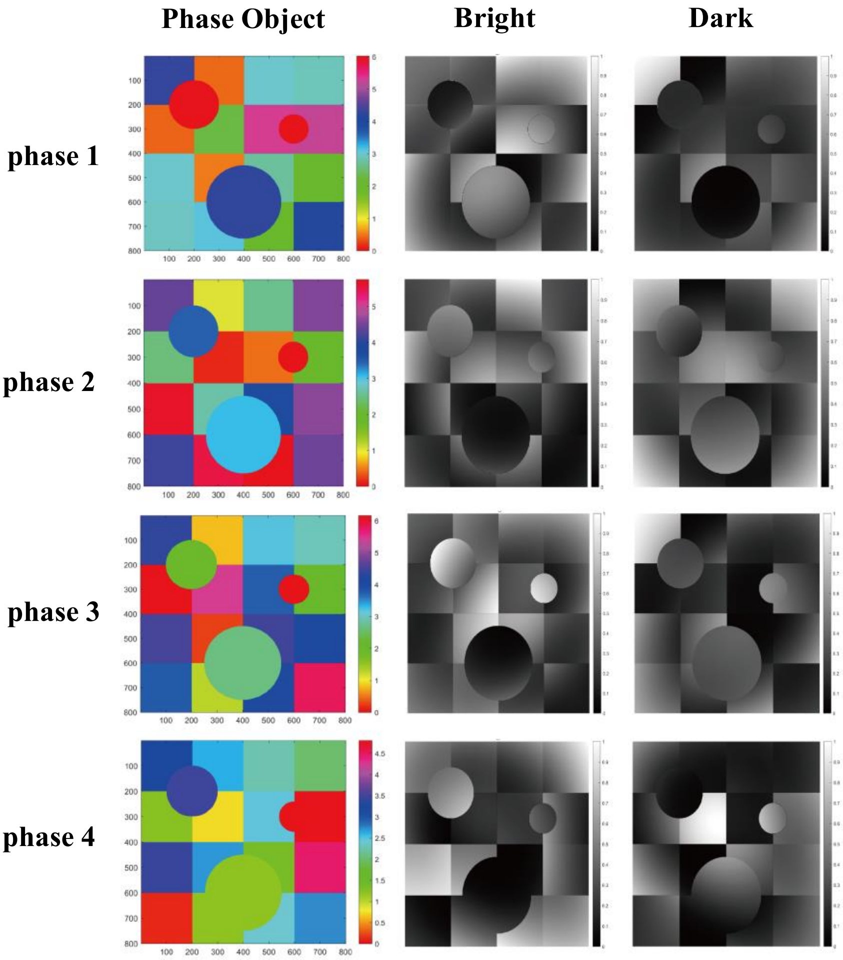

Fig. S5 Simulated phase contrast imaging of a complex-phase object with random phases. Simulations were performed under 780 nm illumination, demonstrating the method's capability to resolve fine structural details regardless of phase complexity.

References

1. Clauser, J. F., Horne, M. A., Shimony, A. & Holt, R. A. Proposed experiment to test local hidden-variable theories. *Phys. Rev. Lett.* **23**, 880–884 (1969).

2. Weihs, G., Jennewein, T., Simon, C., Weinfurter, H. & Zeilinger, A. Violation of bell's inequality under strict einstein locality conditions. *Phys. Rev. Lett.* **81**, 5039–5043 (1998).